

Molecular Level Synthesis of InFeO₃ and InFeO₃/Fe₂O₃ Nanocomposites

Vanessa Nahrstedt, Daniel Stadler, Thomas Fischer, Tomáš Duchoň, David N. Mueller, Claus M. Schneider, and Sanjay Mathur*

Cite This: *Inorg. Chem.* 2021, 60, 3719–3728

Read Online

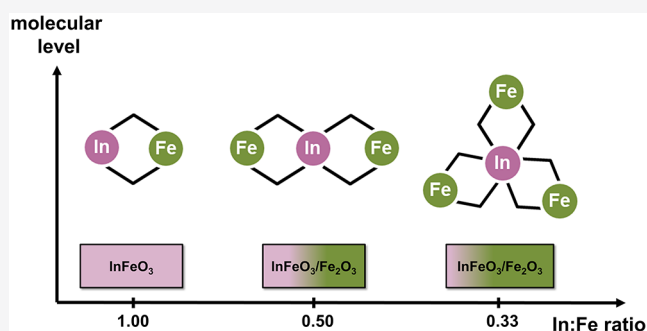
ACCESS |

Metrics & More

Article Recommendations

Supporting Information

ABSTRACT: New heterometallic In–Fe alkoxides [InFe(O^tBu)₄(PyTfP)₂] (1), [InFe₂(O^{neo}Pen)₉(Py)] (2), and [InFe₃(O^{neo}Pen)₁₂] (3) were synthesized and structurally characterized. The arrangement of metal centers in mixed-metal framework was governed by the In:Fe ratio and the coordination preferences of Fe(III) and In(III) centers to be in tetrahedral and octahedral environments, respectively. 3 displayed a star-shaped so-called “Mitsubishi” motif with the central In atom coordinated with three tetrahedral {Fe(O^{neo}Pen)₄}[−] anionic units. The deterministic structural influence of the larger In atom was evident in 1 and 2 which displayed the coordination of neutral coligands to achieve the desired coordination number. Thermal decomposition studies



of compounds 1–3 under inert conditions with subsequent powder diffraction studies revealed the formation of Fe₂O₃ and In₂O₃ in the case of 3 and 2, whereas 1 intriguingly produced elemental In and Fe. In contrary, the thermal decomposition of 1–3 under ambient conditions produced a ternary oxide, InFeO₃, with additional Fe₂O₃ present as a secondary phase in a different stoichiometric ratio predetermined through the In:Fe ratio in 2 and 3. The intimate mixing of different phases in InFeO₃/Fe₂O₃ nanocomposites was confirmed by transmission electron microscopy of solid residues obtained after the decomposition of 1 and 2. The pure InFeO₃ particles demonstrated ferromagnetic anomalies around 170 K as determined by temperature-dependent field-cooled and zero-field-cooled magnetization experiments. A first-order magnetic transition with an increase in the ZFC measurements was explained by temperature-induced reduction of the Fe–Fe distance and the corresponding increase in superexchange.

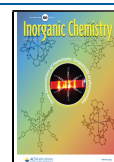
INTRODUCTION

Heterometallic alkoxides are intrinsically efficient precursors to mixed-metal oxides due to preformed heterometallic bridges connected through the alkoxide oxygen (–M–(O)R–M'–) which generally allows their conversion to desired oxide ceramics without lengthy heat treatments since the formation of solid-state phases is not only driven by Fickian diffusion. The selective conversion of a large number of metal alkoxides to ternary ceramics and composites has been demonstrated to verify the role precursor chemistry plays in the synthesis of phase pure material.^{1,2,11–20,3,21–24,4–10} The formation of nanoscaled composites from molecular sources allows to tailor the material properties not possible by conventional synthesis methods, which generally lead to elemental segregation and phase separation. The sol–gel processing and gas phase depositions of monometallic metal alkoxides as single-source precursors are comprehensively studied; however, mixed-metal compositions are relatively less investigated.^{4,7–9,11,12,15,25–45} Despite the potential advantages of chemical processing, the major constraint in the application of heterometallic alkoxides is related to their limited synthetic access and dearth of structural data on metal alkoxide frameworks.

Among binary oxides, ternary ferrites of general formula MFeO₃ (M = In, Y, Eu–Lu) are of fundamental interest because of their physical and structural properties.^{46,47} Recently, thin films of InFeO₃ ($E_g = 2.5$ eV), prepared via pulsed laser deposition, were considered as photoelectrodes for water-splitting reactions by visible and ultraviolet light.⁴⁸ In addition, the LiNbO₃ type of InFeO₃ is a room-temperature polar magnet that shows the functional properties of small tolerance-factor perovskites and is of fundamental interest because of the canted G-type antiferromagnetic ordering of Fe³⁺ moments.^{49–51} In the realm of mixed-metal iron–indium oxides, the antiferromagnet InFe₂O₄ is isostructural to LuFe₂O₄, which shows electrical polarization⁵² and charge as well as magnetic ordering phenomena between 230 and 250 K, whereas (In_{1–x}Fe_x)₂O₃ phases show ferromagnetism at room temperature.^{53,54} We

Received: November 24, 2020

Published: February 23, 2021



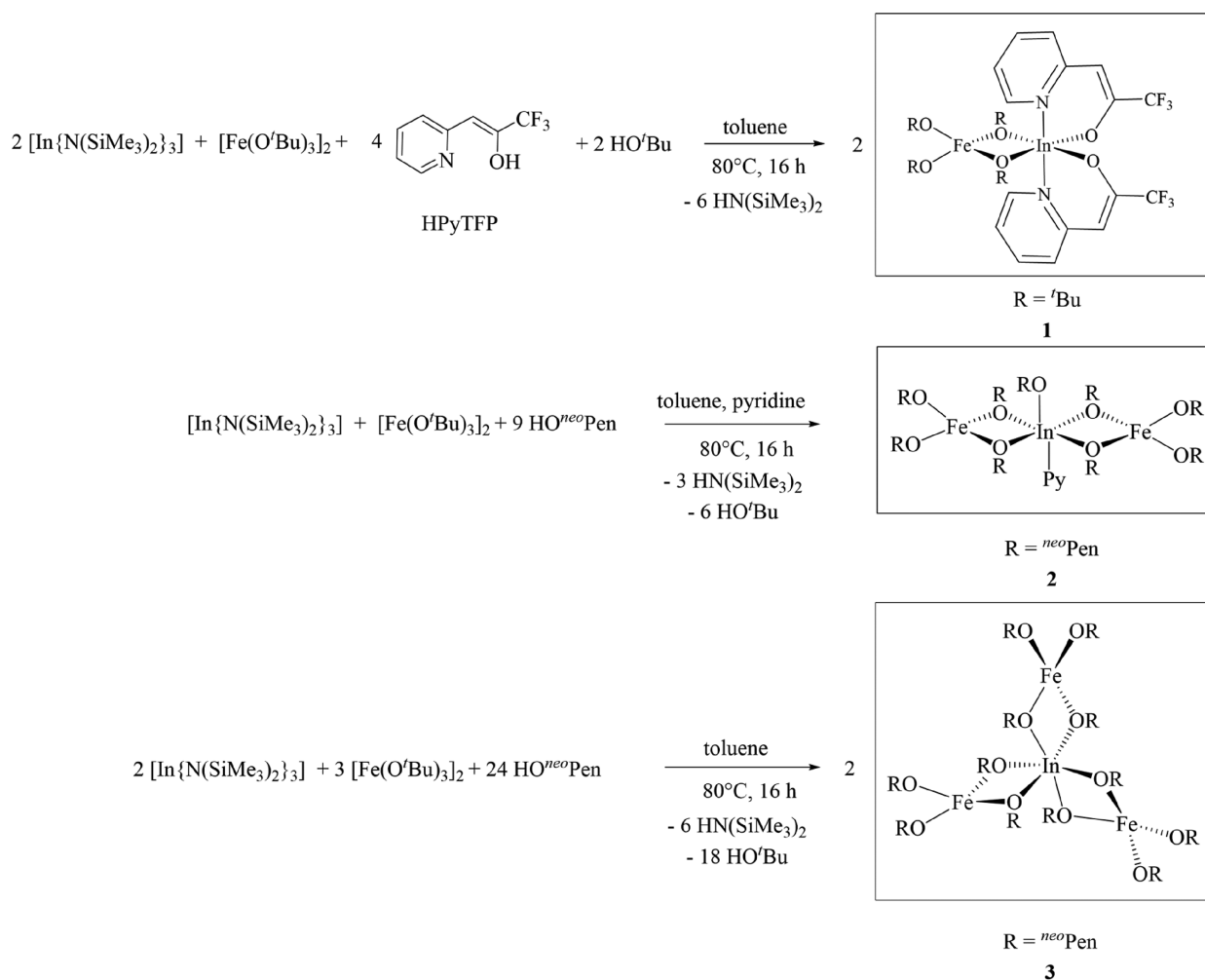


Figure 1. Schematic synthesis of heterometallic alkoxides $[\text{InFe}(\text{O}^t\text{Bu})_4(\text{PyTFP})_2]$ (1), $[\text{InFe}_2(\text{O}^{neo}\text{Pen})_9(\text{Py})]$ (2), and $[\text{InFe}_3(\text{O}^{neo}\text{Pen})_{12}]$ (3).

report here the synthesis and characterization of a new series of mixed metal alkoxide precursors $[\text{InFe}(\text{O}^t\text{Bu})_4(\text{PyTFP})_2]$ (1), $[\text{InFe}_2(\text{O}^{neo}\text{Pen})_9(\text{Py})]$ (2), and $[\text{InFe}_3(\text{O}^{neo}\text{Pen})_{12}]$ (3) as well as their transformation into InFeO_3 for 1 and $\text{InFeO}_3/\text{Fe}_2\text{O}_3$ composites for 2 and 3.

RESULTS AND DISCUSSION

The new series of mixed-metal alkoxides 1–3 were obtained by *in situ* alcoholysis of $[\text{In}\{\text{N}(\text{SiMe}_3)_2\}_3]$ in the presence of iron(III) *tert*-butoxide ($[\text{Fe}(\text{O}^t\text{Bu})_3]_2$) and pyridine for 2 as well as the chelating anionic ligand HPyTFP in the case of 1 (Figure 1). The molecular structures of 1–3 were confirmed by single-crystal X-ray diffraction analysis (Figure 2).

The molecular structures of 1–3 show iron in a 4-fold coordination of oxygen atoms formed by two terminal and two μ_2 -bridging alkoxy ligands. Irrespective of the metal ratio (1:1, 1:2, and 1:3), $\{\text{Fe}(\text{OR})_4\}^-$ units ($\text{R} = ^{neo}\text{Pen}$ (2, 3), ^tBu (1)) coordinate to the indium center in a bidentate fashion in all three compounds. $[\text{InFe}_3(\text{O}^{neo}\text{Pen})_{12}]$ (3) with an In:Fe stoichiometry of 1:3 was found to consistently produce the “Mitsubishi” motif with the central indium atom, coordinated by three bidentate $\{\text{Fe}(\text{O}^{neo}\text{Pen})_4\}^-$ units. The compounds based on an In:Fe ratio of 1:1 and 1:2 displayed in 1 and 2, respectively, highlighted the necessity of the coordination of both neutral or anionic coligands to form stable frameworks. $[\text{InFe}_2(\text{O}^{neo}\text{Pen})_9(\text{Py})]$ 2 displayed a linear arrangement of indium

and iron centers with Fe present in characteristic tetrahedral coordination. The octahedral coordination preferred by indium atoms is achieved by a neutral pyridine ligand in $[\text{InFe}_2(\text{O}^{neo}\text{Pen})_9(\text{Py})]$ (2) to ensure the preferred octahedral environment by the larger In(III) ($r(\text{Fe}^{3+}) = 65 \text{ pm}$ and $r(\text{In}^{3+}) = 80 \text{ pm}$).⁵⁵ Attempts directed to obtain “donor-free” indium–iron complexes with 1:1 ratio were not successful, possibly due to the structural preferences observed in 2 and 3. The incorporation of the anionic ligand HPyTFP, which has been used for stabilizing a large number of metals through its bidentate chelation, was found to increase the stability of the heterometallic framework based on the 1:1 ratio between In and Fe which resulted in the formation of 1.^{32,56–63} The chelating ligand is coordinated to the indium metal center due to the larger ionic radius of indium.⁵⁵ However, the use of chelating ligands in the construction of heterometallic alkoxides represents a delicate interplay between the driving force for the formation of mixed metal assemblies and the stabilization of monometallic species. For example, an increased amount of HPyTFP supports the formation of homometallic $[\text{Fe}(\text{O}^t\text{Bu})_2(\text{PyTFP})_2]$, which was not observed in this study.

The suitability of 1–3 in the formation of In–Fe–O ceramics was evaluated by thermogravimetric studies (Figure 3) for which the samples were gradually heated to 600 °C under a dry nitrogen atmosphere. Thermogravimetric measurements of 2 and 3 revealed multistep decomposition in each case that can be

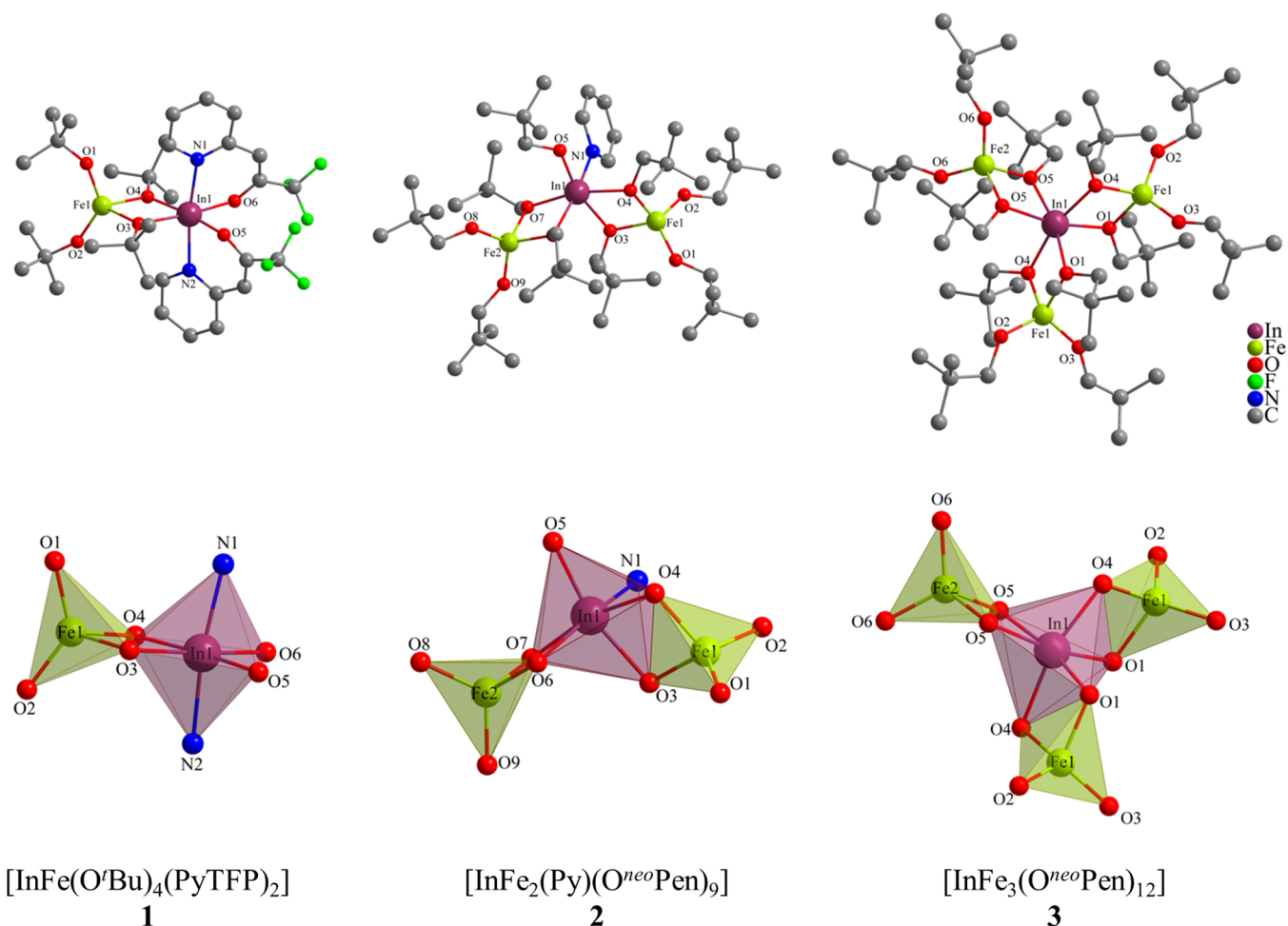


Figure 2. Molecular structures of $[\text{InFe}(\text{O}^t\text{Bu})_4(\text{PyTFP})_2]$ (1), $[\text{InFe}_2(\text{Py})(\text{O}^{neo}\text{Pen})_9]$ (2), and $[\text{InFe}_3(\text{O}^{neo}\text{Pen})_{12}]$ (3) with different indium iron ratios as well as the coordination polyhedral of indium and iron; hydrogen atoms are omitted for clarity.

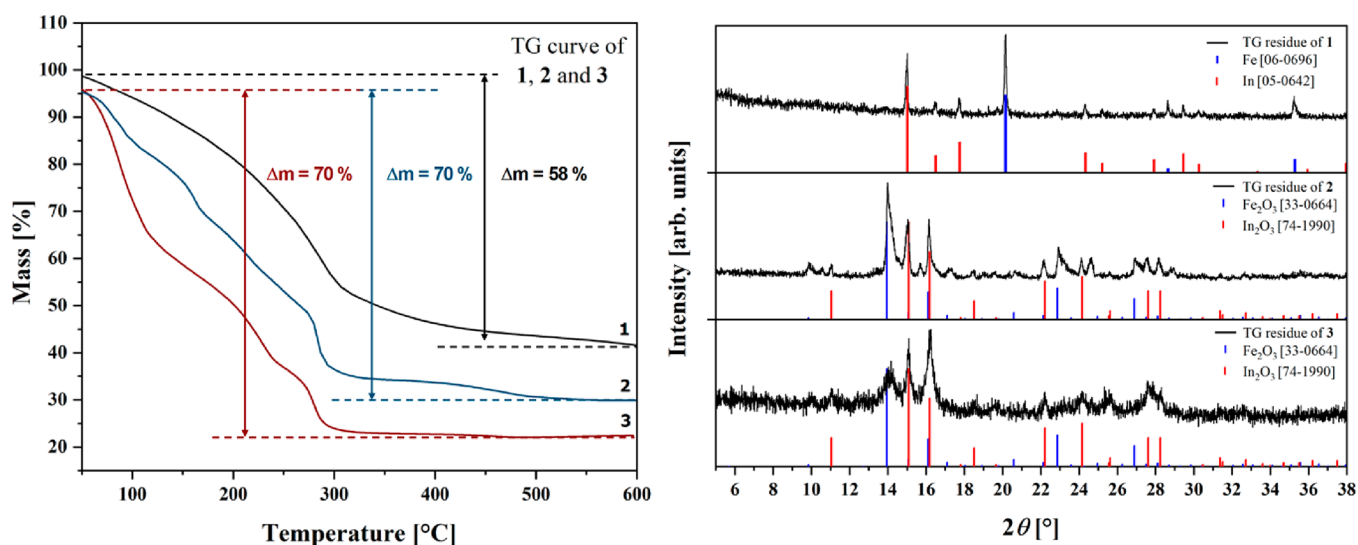


Figure 3. Thermogravimetry measurements of 1–3 up to 600 °C under a N_2 atmosphere (left) and powder XRD of the residue after the measurements with literature data for Fe_2O_3 [33-0664], Fe [06-0696] in blue and In_2O_3 [74-1990], In [05-0642] in red (right).

ascribed to the sequential decomposition of ligands of different chemical strengths (alkoxide vs alkenolate) present on different metal centers (In and Fe) to finally produce $\text{In}_2\text{O}_3/\text{Fe}_2\text{O}_3$ composites, which were analyzed by powder XRD studies

(Figure 3). The deviation of observed (2: $\Delta m(\text{exp}) = 70\%$; 3: $\Delta m(\text{exp}) = 69\%$) and calculated mass loss (2: $\Delta m(\text{calc}) = 60\%$; 3: $\Delta m(\text{calc}) = 67\%$) regarding the formation of $\text{In}_2\text{O}_3/\text{Fe}_2\text{O}_3$ composite can be attributed to partial hydrolysis of the

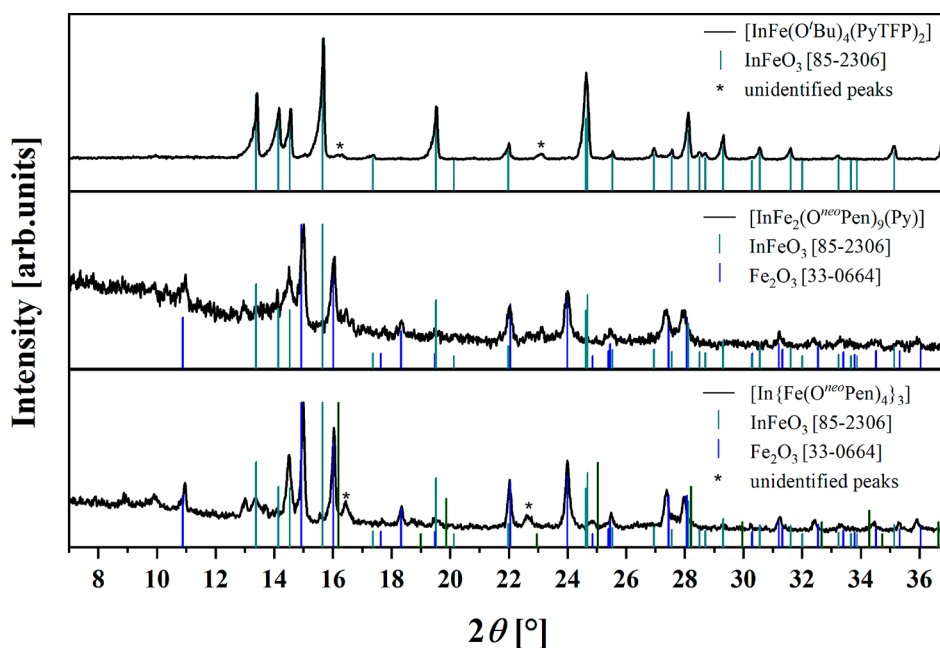


Figure 4. XRD plots of 1–3 after thermal decomposition at 1000 °C for 16 h with a heating rate of 300 °C/h.

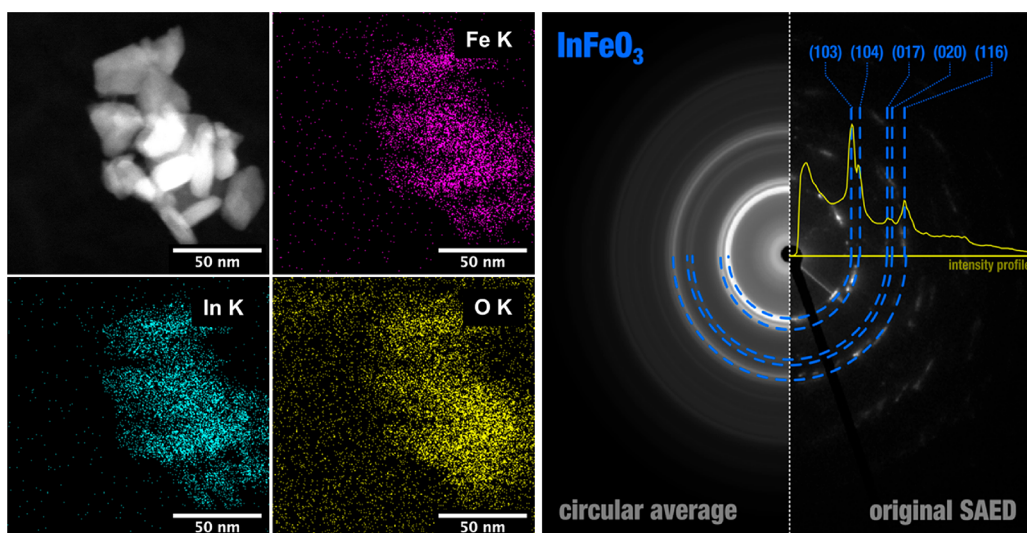


Figure 5. TEM images of 1 after thermal decomposition at 1000 °C with EDX mapping regarding indium (cyan), iron (magenta), and oxygen (yellow) as well as SAED pattern and circular averaged pattern with indexed InFeO_3 reflexes (blue for [85-2306]). The intensity profile (yellow) highlights all diffraction intensity of the circular averaged data.

heterometallic alkoxides during the transfer of the samples from the flasks to the alumina crucibles used in TG/DTA analyses. In contrast, thermogravimetric decomposition of the heterometallic alkoxide with a 1:1 metal ratio (**1**) led to the formation of $\text{In}(0)$ and $\text{Fe}(0)$ with a mass loss of 58%, which might be due to the reduction of metal centers by the ligands. The redox activity of the heteroarylalkenolate ligands was observed for several metals before, e.g., cobalt and tin.^{61,64} With regard to monometallic cobalt precursors $[\text{Co}^{\text{II}}(\text{PyTFP})_2(\text{DMAP})]$ (DMAP = 4-(dimethylamino)pyridine) and $[\text{Co}^{\text{III}}(\text{PyTFP})_3]$, the HPyTFP ligand caused not only the oxidation of the metal center (Co^{II} to Co^{III}) but also the reduction of Co^{III} to Co^{II} during gas phase deposition to synthesize Co_3O_4 .

In contrast to the chemical composition of the residual solids obtained upon performing the thermal decomposition under inert conditions, heating 1–3 in air at 1000 °C for 16 h with a

heating rate of 300 °C/h produced ternary InFeO_3 (**1**), which was proven by XRD measurements (Figure 4). The additional $\alpha\text{-Fe}_2\text{O}_3$ phase was formed in **2** and **3** due to an excess amount of iron present in $[\text{InFe}_2(\text{O}^{\text{neo}}\text{Pen})_9(\text{Py})]$ (**2**) and $[\text{InFe}_3(\text{O}^{\text{neo}}\text{Pen})_{12}]$ (**3**). In the case of **1**, low-intensity peaks were observed around 23.2°, 23.5°, 16.4°, and 16.5°, which could not be assigned to any expected phase of iron or indium oxides or their mixtures. Also, the formation of metal carbides can be ruled out based on the differential peak analysis with the powder diffraction files available in the databank.

The existence of crystalline phase as observed in the TEM data (Figure 5) and the identification of InFeO_3 as the crystalline phase (XRD analysis) suggested the preferential crystallization of InFeO_3 formed upon the decomposition of molecular precursor. Hence, it can be assumed that because of chemically preorganized arrangement of the metal centers in **1**, its

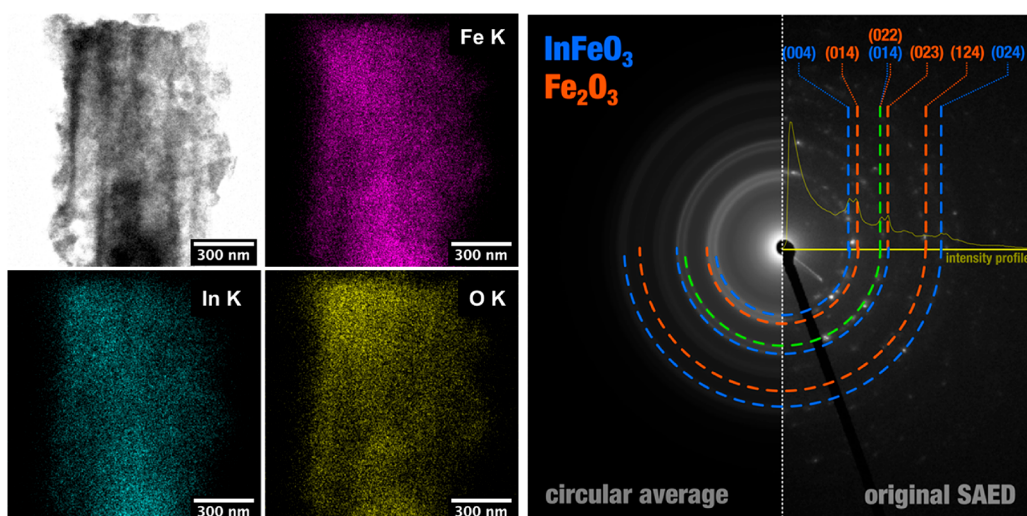


Figure 6. TEM images of **2** after thermal decomposition at 1000 °C with EDX mapping regarding indium (cyan), iron (magenta), and oxygen (yellow) as well as the SAED pattern and circular averaged pattern with indexed InFeO_3 (blue for [85-2306]) and Fe_2O_3 (orange for [33-0664]) reflexes. The intensity profile (yellow) highlights all diffraction intensity of the circular averaged data.

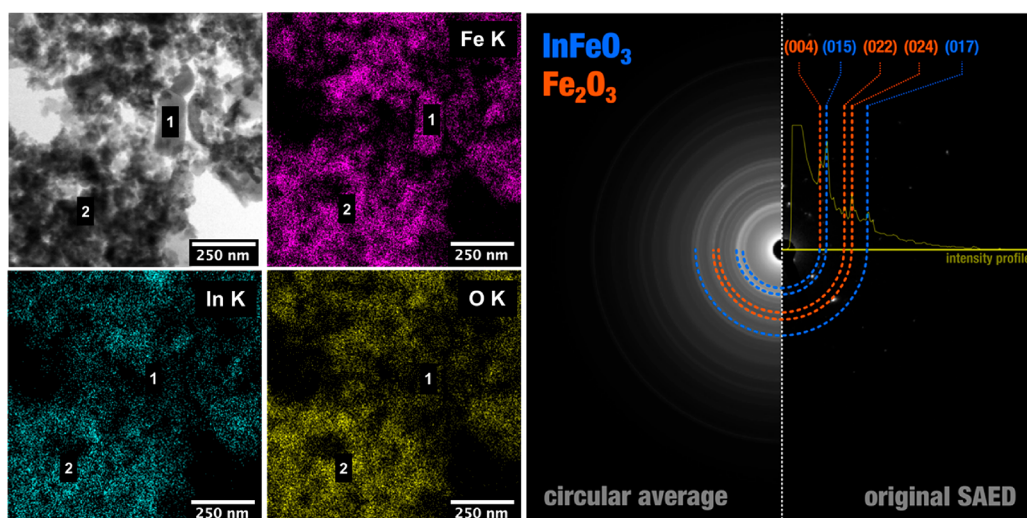


Figure 7. TEM images of **3** after thermal decomposition at 1000 °C with EDX mapping regarding indium (cyan), iron (magenta), and oxygen (yellow) as well as the SAED pattern and circular averaged pattern with indexed InFeO_3 (blue for [85-2306]) and Fe_2O_3 (orange for [33-0664]) reflexes. The intensity profile (yellow) highlights all diffraction intensity of the circular averaged data.

decomposition by heat treatment did not lead to segregation into iron and indium regions that ultimately would lead to the formation of iron and indium oxide phases. In contrast, only hexagonal InFeO_3 was observed in XRD (Figure 4), EDX, and SAED measurements (Figure 5), which is a validation of the hypothesis that the initial chemical configuration present in the precursor molecule is maintained during the thermal treatment.

TEM characterization of $\text{InFeO}_3/\text{Fe}_2\text{O}_3$ composites, synthesized by thermal decomposition of **2** and **3** at 1000 °C, showed agglomerated nanoparticles consisting of both InFeO_3 and Fe_2O_3 (Figures 6 and 7). A similar phase separation was observed in the decomposition of $[\text{NdAl}_3(\text{OR})_{12}]$ which produced NdAlO_3 as the crystalline phase embedded in an amorphous alumina matrix.^{5,65} The decomposition product of precursor **2** revealed a homogeneous distribution of In, Fe, and O (EDX, Figure 6), indicating the homogeneous formation of ternary InFeO_3 and Fe_2O_3 phases that was also observed in TEM images. In addition, the existence of both InFeO_3 and Fe_2O_3 was verified by the SAED study, represented in Figure 6.

TEM images of the solid material obtained upon the decomposition of precursor **3** demonstrated different particle morphologies when compared to the decomposition product of **2** (Figure 7). In some areas (e.g., spot 1) a lower concentration of indium, but a higher concentration of iron, is present, representing the cocrystallization of InFeO_3 and $\alpha\text{-Fe}_2\text{O}_3$ particles, which was also observed in SAED measurement (Figure 7, right). Whereas in other spots (e.g., spot 2), a homogeneous distribution of In, Fe, and O exists, which indicates no formation of hematite in that area.

Further magnetic and spectroscopic analysis was done for the decomposition product of **1**, which did not show any hematite impurities in the XRD. The Mössbauer spectrum (Figure 8) showed characteristic absorption features of InFeO_3 with a strong doublet and additional weak sextet splitting that was confirmed by fitting parameters (Figure 8, table) that are in line with values reported for InFeO_3 .^{47,66}

X-ray absorption spectroscopy performed at room temperature revealed the electronic structure of the material (Figure 9).

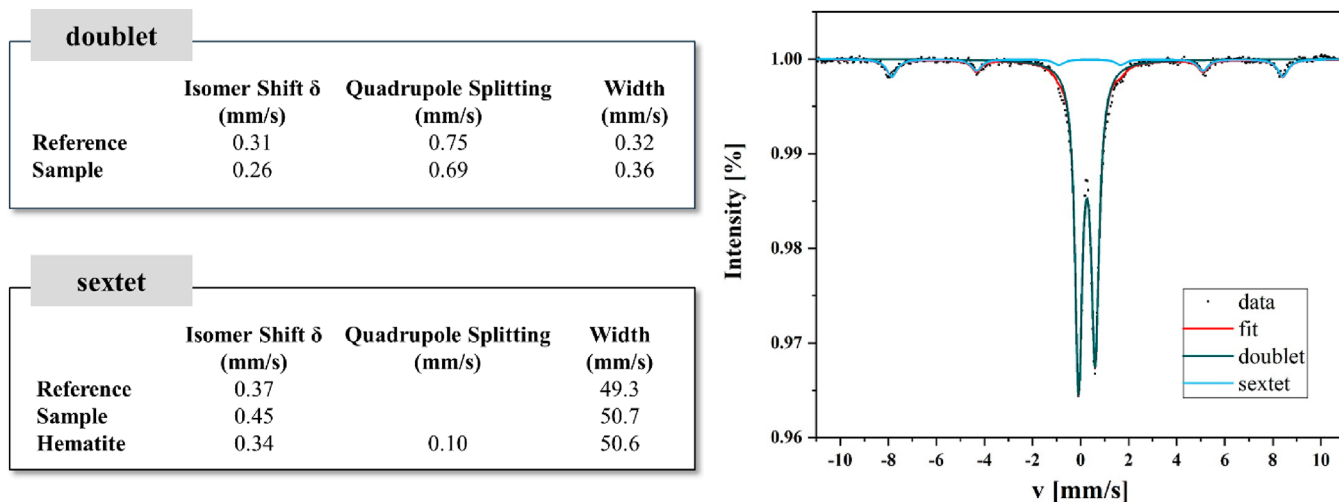


Figure 8. Mössbauer spectroscopy of decomposed 1 (black: sample; red: fit; green: doublet; blue: sextet) with values for the isomer shift, quadrupole splitting, and width for the sample as well as literature references.^{47,67}

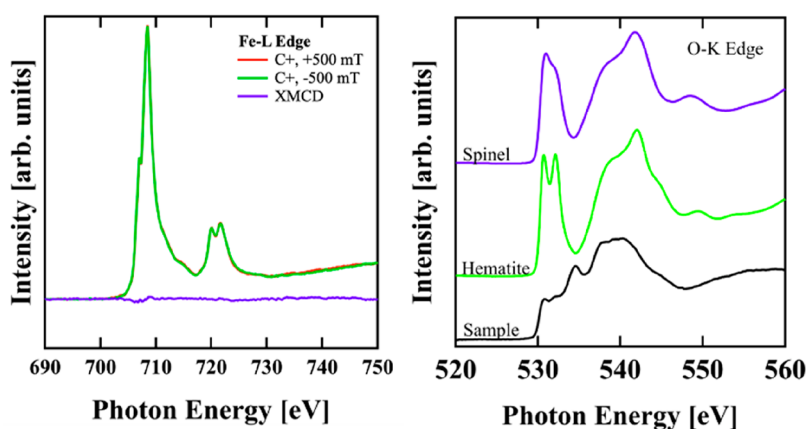


Figure 9. X-ray absorption spectrum of 1 (left: Fe-L_{2/3} edge; right: O-K edge) with hematite and magnetite reference spectra.

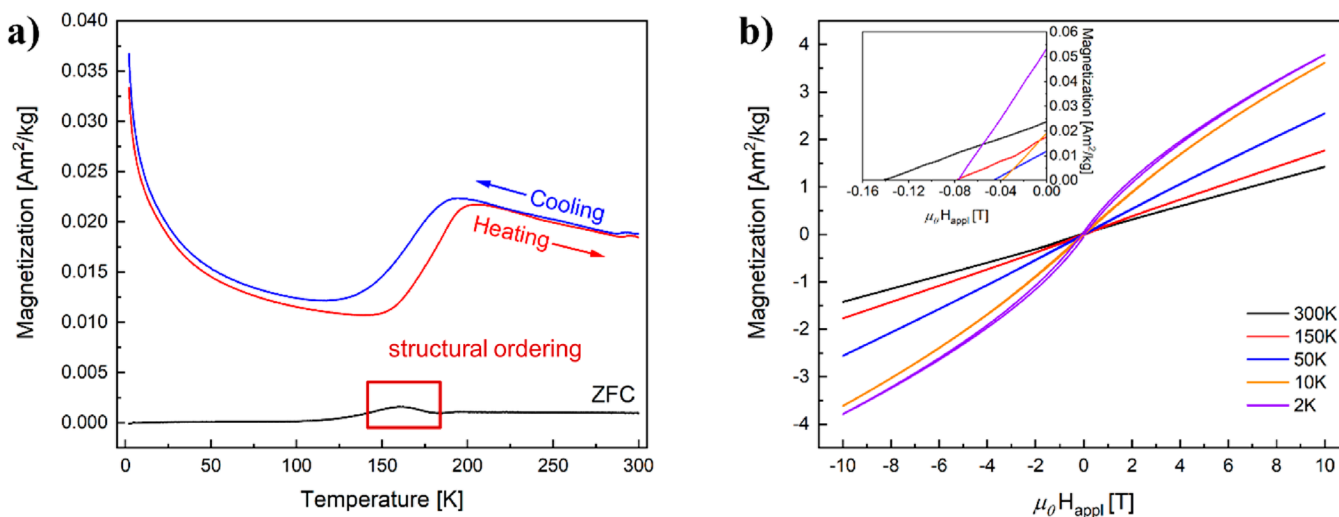


Figure 10. Field-cooled (FC, blue and red line) and zero-field-cooled (ZFC) measurements (a) and magnetic hysteresis curves (b) at different temperatures of the InFeO₃ powder, obtained from 1.

The Fe-L_{3,2} edge showed the distinct pre-edge feature at 707.1 eV of approximately half the intensity of the white line found for iron in the trivalent oxidation state in iron oxide (Figure 9, left).^{68,69} Besides hematite, which was already excluded by XRD

measurement, the existence of the spinel phase could not be observed in the O-K edge, which showed no characteristic absorption features for hematite or magnetite in the pre-edge region compared to the reference spectrum (Figure 9, right). In

Table 1. Summary of Crystallographic and Refinement Data for Compounds 1–3

	1	2	3
formula	InFeC ₃₂ H ₄₆ O ₆ N ₂ F ₆	InFe ₂ C ₅₀ H ₁₀₄ O ₉ N	InFe ₃ C ₆₀ H ₁₃₂ O ₁₂
<i>M</i> [g mol ⁻¹]	839.4	1089.9	1328.1
crystal system	triclinic	monoclinic	monoclinic
space group	$P\bar{1}$	$P2_1/c$	$P2/n$
<i>a</i> [Å]	8.90(8)	11.89(2)	11.35(7)
<i>b</i> [Å]	13.82(1)	42.86(6)	17.33(8)
<i>c</i> [Å]	16.44(1)	38.10(7)	19.96(1)
α [deg]	88.1(6)	90	90
β [deg]	81.6(6)	95.70(2)	102.18(5)
γ [deg]	77.0(6)	90	90
<i>V</i> [Å ³]	1949.0(3)	19315.2(6)	3838.2(4)
<i>Z</i>	2	12	2
reflections collected	18866	32388	43190
independent reflections	8213	19944	6776
observed reflections	3771	1783	3495
goodness of fit	0.979	1.004	0.879
<i>R</i> (int)	0.111	0.093	0.200
<i>R</i> ₁ , <i>wR</i> ₂ [<i>I</i> > 2σ(<i>I</i>)]	0.089, 0.245	0.086, 0.231	0.061, 0.132
<i>R</i> ₁ , <i>wR</i> ₂ (all data)	0.172, 0.285	0.121, 0.258	0.132, 0.163

contrast, the sample revealed absorption maxima at 530.8, 531.1, 534.6, and 538.1 eV, which are also known for hexagonal manganates (RMnO₃, with R = Y, Ln). These findings are in line with Mössbauer spectroscopy and XRD. However, the signals are broadened in contrast to spectra from a single-crystalline hexagonal manganate.^{70,71}

Temperature- (Figure 10a) and field-dependent (Figure 10b) magnetization measurements at lower temperatures of phase pure InFeO₃ powders revealed Curie-like paramagnetism and a signal around 160 K (Figure 10, left, red box) in the zero-field-cooled (ZFC) curve with a drop-in magnetization during field-cooled (FC) measurements, that indicates a first-order magnetic phase transition. During cooling, the decrease in magnetization was seen at 175 K, while the very same phase transition was observed at 200 K during heating.

Field-dependent magnetization measurements at temperatures ranging from 300 to 2 K revealed a paramagnetic behavior at room temperature and the appearance of a hysteresis below 150 K, which was also described for epitaxially grown InFeO₃ on ZnO(001) via pulsed laser deposition.⁷² Even though the magnetic anomaly in ZFC measurements was not observed for those films, the trend of spontaneous magnetization in ZFC measurements was reported for polycrystalline hexagonal ferrites and manganates with the same symmetry.⁷³ In these reports, an increased exchange interaction between the Fe³⁺ atoms in the hexagonal is stated to cause the observed signal in the ZFC curve.⁷⁴

CONCLUSION

Successful synthesis of heterometallic alkoxides ([InFe(O^{*t*}Bu)₄(PyTFP)₂] (1), [InFe₂(O^{*neo*}Pen)₉(Py)] (2), and [InFe₃(O^{*neo*}Pen)₁₂] (3)) allowed a molecular access to single-phase InFeO₃ (1) and InFeO₃/Fe₂O₃ nanocomposites (2 and 3). The cation stoichiometry in the precursors was deterministic for the formation of a ternary single-phase material and oxide–oxide nanocomposite originating from single molecule sources. Thermal gravimetric studies in conjunction with powder X-ray diffraction and electron microscopy provided insight into the formation of chemically homogeneous precursors through the preorganized atomic arrangements and the thermodynamically

induced phase formation (or separation) observed upon heat treatment. The preferred crystallization of the perovskite phase in the case of InFeO₃/Fe₂O₃ nanocomposites is probably due to the miscibility limits and favorable enthalpy of formation. Magnetic measurements of the material revealed a first-order magnetic transition with an increase of the magnetization in the ZFC measurements that was explained by temperature-induced reduction of the Fe–Fe distance and the corresponding increase in superexchange. Recently, band gap calculations (*E*_g = 2.5 eV) and photoelectrochemical characterizations of InFeO₃ emphasized its water splitting potential by visible and ultraviolet light.⁴⁸

EXPERIMENTAL SECTION

General Procedure. All syntheses were performed under an inert nitrogen gas atmosphere by using a Stock glass vacuum line. If not mentioned, all reagents were used without further purification. Used solvents were freshly distilled and dried over sodium. Suitable crystals for X-ray diffraction analysis were obtained by recrystallization in toluene at –18 °C for compounds 1–3. The crystallographic data for all compounds are summarized in Table 1. The data collection for X-ray structure elucidation was performed on a STOE IPDS II diffractometer (Mo *K*α = 0.71073 Å, 50 kV, 30 mA), and the used programs for structure solution as well as the refinement are SIR-92,⁷⁵ SHELXS,⁷⁶ SHELXL,⁷⁶ and WinGX.^{77,78} Elemental analysis was performed by using a HEKAtech CHNS Euro EA 3000 analyzer. TG analysis was performed by a TG/DSC1 (Mettler Toledo GmbH, Germany) apparatus using nitrogen gas and a heating rate of 10 °C/min. Powder X-ray diffraction was measured on a STOE diffractometer with STADI MP system and either Mo *K*α (*λ* = 0.71 Å) or Cu *K*α radiation (*λ* = 1.54 Å). TEM characterizations with selected-area electron diffraction (SAED) as well as energy-dispersive X-ray (EDX) studies of particle dispersions (toluene/isopropyl alcohol 1:1) were performed on a JEOL JEM-2200FS transmission electron microscope operated at an acceleration voltage of 200 kV. SAED analyses were performed using the software CrysTBox 1.10.⁷⁹ Mössbauer spectroscopy was measured on a Wissel spectrometer at ambient temperature. XAS measurements were performed at the soft X-ray undulator beamline UES6/1-SGM at the synchrotron facility BESSY II in Berlin.

Precursor Synthesis. [In(*N*(SiMe₃)₂)₃]. Bis(trimethylsilyl)amine (15.51 mL, 75 mmol) was cooled in liquid nitrogen and covered with a layer of *n*-BuLi (2.5 M heptane, 30.00 mL, 75 mmol). After thawing, the mixture was slowly added to a solution of InCl₃ (5.50 g, 25 mmol) in dry THF (50 mL). The suspension was stirred for 3 h. Afterward, the

solvent was removed under reduced pressure, and $[\text{Li}\{\text{N}(\text{SiMe}_3)\}]$ was sublimated at 90 °C in vacuo (10^{-2} mbar) followed by sublimation of the crude product at 110 °C in vacuo (10^{-2} mbar). The resulting colorless solid was used for the next syntheses without further analysis; yield 12.24 g (22 mmol, 88%). Molar mass: 563.89 g mol⁻¹.

$[\text{Fe}(\text{O}^i\text{Bu})_3]_2 \cdot \text{FeCl}_3$ (6.23 g, 38 mmol) in toluene (50 mL) was cooled in liquid nitrogen, and THF (150 mL) was slowly added. The mixture was stirring while thawing. Afterward, a solution of KO^tBu (12.8 g, 114 mmol) in THF (150 mL) was added. The mixture was stirred for 24 h at 80 °C and after that cooled to room temperature. The solvent was removed under reduced pressure, and the crude product was sublimated at 90 °C in vacuo (10^{-2} mbar), resulting in a green solid; yield 14.22 g (26 mmol, 68%). The product was used for the next step without further analysis. Molar mass: 550.38 g mol⁻¹; calcd: C 52.4, H 9.8; found: C 51.2, H 9.9.

$[\text{InFe}(\text{O}^i\text{Bu})_4(\text{PyTFP})_2]$ (1). $[\text{Fe}(\text{O}^i\text{Bu})_3]_2$ (0.35 g, 0.63 mmol) was solved in toluene (6 mL), and 1 equiv of PyTFP (0.12 g, 0.63 mmol) was added. Afterward, a solution of $[\text{In}\{\text{N}(\text{SiMe}_3)_2\}_3]$ (0.71 g, 1.27 mmol) in toluene (6 mL) was added to the reaction mixture. The solution was stirred at 100 °C overnight, and yellow crystals were obtained at -18 °C, which revealed the formation of 1; yield 0.32 g (0.38 mmol, 61%). C₃₂H₄₆FeInN₂O₆ (839.4 g mol⁻¹): calcd: C 45.8, H 5.5, N 3.3; found: C 46.9, H 6.4, N 3.5.

$[\text{InFe}_2(\text{O}^{neo}\text{Pen})_9(\text{Py})]$ (2). For the preparation of $[\text{InFe}_2(\text{O}^{neo}\text{Pen})_9(\text{Py})]$, $[\text{In}\{\text{N}(\text{SiMe}_3)_2\}_3]$ (0.38 g, 0.64 mmol) in toluene (4 mL) was added to a solution of $[\text{Fe}(\text{O}^i\text{Bu})_3]_2$ (0.33 g, 0.60 mmol) in toluene (6 mL). Afterward, pyridine (4 mL) and neopentanol (10 mL) were added. The orange solution was stirred overnight at 60 °C, and yellow crystals were obtained at -18 °C; yield 0.55 g (0.51 mmol, 79%). C₅₀H₁₀₄Fe₂InNO₉ (1089.9 g mol⁻¹): calcd: C 55.1, H 9.6, N 1.3; found: C 53.7, H 9.9, N 1.0.

$[\text{InFe}_3(\text{O}^{neo}\text{Pen})_{12}]$ (3). $[\text{InFe}_3(\text{O}^{neo}\text{Pen})_{12}]$ was synthesized by adding $[\text{In}\{\text{N}(\text{SiMe}_3)_2\}_3]$ (0.12 g, 0.21 mmol) in toluene (4 mL) to a solution of $[\text{Fe}(\text{O}^i\text{Bu})_3]_2$ (0.17 g, 0.31 mmol) in toluene (6 mL), followed by the addition of neopentanol (10 mL). The mixture was stirred for 24 h at 60 °C, and yellow crystals were obtained at -18 °C; yield 0.23 g (0.17 mmol, 83%). InFe₃C₆₀H₁₂₀O₁₂ (1328.1 g mol⁻¹): calcd: C 54.3, H 10.0; found: C 55.6, H 10.2.

Material Synthesis. For material synthesis 100 mg of heterometallic indium iron precursors 1–3 was prepared under inert conditions and transferred in sealed flasks. The thermal decompositions of the green (1) and yellow (2 and 3) solids were performed in air at 1000 °C (16 h) with a heating rate of 300 °C/h.

■ ASSOCIATED CONTENT

Supporting Information

The Supporting Information is available free of charge at <https://pubs.acs.org/doi/10.1021/acs.inorgchem.0c03425>.

Table S1 and Figure S1 (PDF)

Accession Codes

CCDC 2045551 and 2045554–2045555 contain the supplementary crystallographic data for this paper. These data can be obtained free of charge via www.ccdc.cam.ac.uk/data_request/cif, or by emailing data_request@ccdc.cam.ac.uk, or by contacting The Cambridge Crystallographic Data Centre, 12 Union Road, Cambridge CB2 1EZ, UK; fax: +44 1223 336033.

■ AUTHOR INFORMATION

Corresponding Author

Sanjay Mathur – Institute of Inorganic Chemistry, University of Cologne, 50939 Cologne, Germany; orcid.org/0000-0003-2765-2693; Email: sanjay.mathur@uni-koeln.de

Authors

Vanessa Nahrstedt – Institute of Inorganic Chemistry, University of Cologne, 50939 Cologne, Germany; orcid.org/0000-0001-6929-3508

Daniel Stadler – Institute of Inorganic Chemistry, University of Cologne, 50939 Cologne, Germany; orcid.org/0000-0003-3233-9167

Thomas Fischer – Institute of Inorganic Chemistry, University of Cologne, 50939 Cologne, Germany; orcid.org/0000-0002-8363-9613

Tomáš Duchon – PGI-6, Research Centre, Juelich GmbH, 52428 Juelich, Germany

David N. Mueller – PGI-6, Research Centre, Juelich GmbH, 52428 Juelich, Germany; orcid.org/0000-0002-1062-6985

Claus M. Schneider – PGI-6, Research Centre, Juelich GmbH, 52428 Juelich, Germany

Complete contact information is available at:

<https://pubs.acs.org/10.1021/acs.inorgchem.0c03425>

Notes

The authors declare no competing financial interest.

■ ACKNOWLEDGMENTS

This work was funded within the framework of the priority programme SPP1959 of the Deutsche Forschungsgemeinschaft (DFG). The authors thank the University of Cologne and the Excellence Cluster “Quantum Matter and Materials” for the infrastructural support. We also acknowledge the support of Dr. Ingo Pantenburg as well as Ms. Silke Kremer (Core Facility X-ray Crystallography), Mr. Dirk Pullem (Elemental Analysis), and Mr. Fernando Maccari for magnetization measurements (TU Darmstadt, Germany). For Mössbauer spectroscopy we thank Dr. Dominika Zákutná (Charles University, Czech Republic). We thank HZB for the allocation of synchrotron radiation beamtime.

■ REFERENCES

- (1) Mathur, S.; Veith, M.; Rapalaviciute, R.; Shen, H.; Goya, G. F.; Filho, W. L. M.; Berquo, T. S. Molecule Derived Synthesis of Nanocrystalline YFeO₃ and Investigations on Its Weak Ferromagnetic Behavior. *Chem. Mater.* **2004**, *16*, 1906–1913.
- (2) Mathur, S.; Veith, M.; Ruegamer, T.; Hemmer, E.; Shen, H. Chemical Vapor Deposition of MgAl₂O₄ Thin Films Using Different Mg-Al Alkoxides: Role of Precursor Chemistry. *Chem. Mater.* **2004**, *16*, 1304–1312.
- (3) Mathur, S.; Shen, H.; Lecerf, N.; Kjekshus, A.; Fjellvåg, H.; Goya, G. F. Nanocrystalline Orthoferrite GdFeO₃ from a Novel Heterobimetallic Precursor. *Adv. Mater.* **2002**, *14*, 1405–1409.
- (4) Bohr, C.; Yu, P.; Scigaj, M.; Hegemann, C.; Fischer, T.; Coll, M.; Mathur, S. Atomic Scale Growth of GdFeO₃ Perovskite Thin Films. *Thin Solid Films* **2020**, *698*, No. 137848.
- (5) Mathur, S.; Veith, M.; Shen, H.; Hüfner, S.; Jilavi, M. H. Structural and Optical Properties of NdAlO₃ Nanocrystals Embedded in an Al₂O₃ Matrix. *Chem. Mater.* **2002**, *14*, 568–582.
- (6) Veith, M.; Mathur, S.; Lecerf, N.; Bartz, K.; Heintz, M.; Huch, V. Synthesis of NdAlO₃/Al₂O₃ Ceramic-Ceramic Composite by Single-Source Precursor CVD. *Chem. Mater.* **2000**, *12*, 271–274.
- (7) Ojelere, O.; Graf, D.; Mathur, S. Molecularly Engineered Lithium-Chromium Alkoxide for Selective Synthesis of LiCrO₂ and Li₂CrO₄ Nanomaterials. *Inorganics* **2019**, *7*, 22.
- (8) Jamil, A.; Schläfer, J.; Gönüllü, Y.; Lepcha, A.; Mathur, S. Precursor-Derived Rare Earth Metal Pyrochlores: Nd₂Sn₂O₇ Nanofibers and Thin Films As Efficient Photoabsorbers. *Cryst. Growth Des.* **2016**, *16*, S260–S267.
- (9) Mathur, S.; Cavelius, C.; Moh, K.; Shen, H.; Bauer, J. Cobalt Ferrite Nanoparticles from Single and Multi-Component Precursor Systems. *Z. Anorg. Allg. Chem.* **2009**, *635*, 898–902.

- (10) Veith, M.; Haas, M.; Huch, V. Single Source Precursor Approach for the Sol-Gel Synthesis of Nanocrystalline ZnFe₂O₄ and Zinc - Iron Oxide Composites. *Chem. Mater.* **2005**, *17*, 95–101.
- (11) Meyer, F.; Hempelmann, R.; Mathur, S.; Veith, M. Microemulsion Mediated Sol – Gel Synthesis of Nano-Scaled MA₂O₄ (M = Co, Ni, Cu) Spinel from Single-Source Heterobimetallic Alkoxide Precursors. *J. Mater. Chem.* **1999**, *9*, 1755–1763.
- (12) Mathur, S.; Cavalius, C.; Shen, H. CoGa₂O₄ Nanoparticles and Films Using a Single Molecular Source. *Z. Anorg. Allg. Chem.* **2009**, *635*, 2106–2111.
- (13) Meyer, F.; Dierstein, A.; Beck, C.; Härtl, W.; Hempelmann, R.; Mathur, S.; Veith, M. Size-Controlled Synthesis of Nanoscaled Aluminum Spinel Using Heterobimetallic Alkoxide Precursors via Water/Oil Microemulsions. *Nanostruct. Mater.* **1999**, *12*, 71–74.
- (14) Kessler, V. G. Molecular Structure Design and Synthetic Approaches to the Heterometallic Alkoxide Complexes. *Chem. Commun.* **2003**, 1213–1222.
- (15) Hubert-Pfalzgraf, L. G. Some Trends in the Design of Homo- and Heterometallic Molecular Precursors of High-Tech Oxides. *Inorg. Chem. Commun.* **2003**, *6*, 102–120.
- (16) Bradley, D. C.; Mehrotra, R. C.; Rothwell, I. P.; Singh, A. *Alkoxo and Aryloxo Derivatives of Metals*; Elsevier: 2001.
- (17) Bradley, D. C. Metal Alkoxides as Precursors for Electronic and Ceramic Materials. *Chem. Rev.* **1989**, *89*, 1317–1322.
- (18) Li, X.; Zhang, B.; Ju, C.; Han, X.; Du, Y.; Xu, P. Morphology-Controlled Synthesis and Electromagnetic Properties of Porous Fe₃O₄ Nanostructures from Iron Alkoxide Precursors. *J. Phys. Chem. C* **2011**, *115*, 12350–12357.
- (19) Gun'ko, Y. K.; Cristmann, U.; Kessler, V. G. Synthesis and Structure of the First FeII Heterometallic Alkoxide [(THF)NaFe(O'Bu)₃]₂ – a Possible Precursor for New Materials. *Eur. J. Inorg. Chem.* **2002**, *2002*, 1029–1031.
- (20) Mishra, S.; Daniele, S. Molecular Engineering of Metal Alkoxides for Solution Phase Synthesis of High-Tech Metal Oxide Nanomaterials. *Chem. - Eur. J.* **2020**, *26*, 9292.
- (21) Gschwind, F.; Crochet, A.; Maudez, W.; Fromm, K. M. From Alkaline Earth Ion Aggregates via Transition Metal Coordination Polymer Networks towards Heterometallic Single Source Precursors for Oxidic Materials. *Chimia* **2010**, *64*, 299.
- (22) Herrig, H.; Hempelmann, R. Microemulsion Mediated Synthesis of Ternary and Quaternary Nanoscale Mixed Oxide Ceramic Powders. *Nanostruct. Mater.* **1997**, *9*, 241–244.
- (23) Boyle, T. J.; Sears, J. M.; Perales, D.; Cramer, R. E.; Lu, P.; Chan, R. O.; Hernandez-Sanchez, B. A. Synthesis and Characterization of Tris(Trimethylsilyl)Siloxide Derivatives of Early Transition Metal Alkoxides That Thermally Convert to Varied Ceramic-Silica Architecture Materials. *Inorg. Chem.* **2018**, *57*, 8806–8820.
- (24) Lu, H.; Wright, D. S.; Pike, S. D. The Use of Mixed-Metal Single Source Precursors for the Synthesis of Complex Metal Oxides. *Chem. Commun.* **2020**, *56*, 854–871.
- (25) Schläfer, J.; Stucky, S.; Tyrra, W.; Mathur, S. Heterobi- and Trimetallic Cerium(IV) Tert -Butoxides with Mono-, Di-, and Trivalent Metals (M = K(I), Ge(II), Sn(II), Pb(II), Al(III), Fe(III)). *Inorg. Chem.* **2013**, *52*, 4002–4010.
- (26) Veith, M.; Grätz, F.; Huch, V. Fe₃O₃(OC₂H₅)₂₁·C₂H₅OH - A New Structure Type of an Uncharged Iron(III) Oxide Alkoxide Cluster. *Eur. J. Inorg. Chem.* **2001**, *2001*, 367–368.
- (27) Veith, M.; Hill, S.; Huch, V. Synthese Und Charakterisierung von In^{III}-Sn^{II}-Halogenido-Alkoxiden und von Indiumtri-tert-butoxid. *Z. Anorg. Allg. Chem.* **2001**, *627*, 1495–1504.
- (28) Spandl, J.; Kusserow, M.; Brüdgam, I. Alkoxo-Verbindungen Des Dreiwertigen Eisen: Synthese Und Charakterisierung von [Fe₂(OtBu)₆], [Fe₂Cl₂(OtBu)₄], [Fe₂Cl₄(OtBu)₂] und [N-(NBu)₄]₂[Fe₆OCl₆(OMe)₁₂]. *Z. Anorg. Allg. Chem.* **2003**, *629*, 968–974.
- (29) Kusserow, M.; Spandl, J. Alkohololyse von [Fe₂(O'Bu)₆] als einfacher Weg zu neuen Eisen(III)-Alkoxo-Verbindungen: Synthesen und Kristallstrukturen von [Fe₂(OtAmyl)₆], [Fe₃OCl(OiPr)₁₂]. *Z. Anorg. Allg. Chem.* **2006**, *632*, 885–892.
- (30) Schläfer, J.; Tyrra, W.; Mathur, S. Erratum: Octakis(tert-butoxo)dicerium(IV) [Ce₂(O' Bu)₈]: Synthesis, Characterization, Decomposition, and Reactivity. *Inorg. Chem.* **2014**, *53*, 2751–2753.
- (31) Veith, M.; Mathur, S.; Shen, H.; Lecerf, N.; Hüfner, S.; Jilavi, M. H. Single-Step Preparation of Oxide - Oxide Nanocomposites: Chemical Vapor Synthesis of LnAlO₃/Al₂O₃ (Ln = Pr, Nd) Thin Films. *Chem. Mater.* **2001**, *13*, 4041–4052.
- (32) Appel, L.; Fiz, R.; Tyrra, W.; Pantenburg, I.; Mathur, S. Design of Volatile Mixed-Ligand Tantalum(V) Compounds as Precursors to Ta₂O₅ Films. *Cryst. Growth Des.* **2015**, *15*, 1141–1149.
- (33) Graf, D.; Schläfer, J.; Garbe, S.; Klein, A.; Mathur, S. Interdependence of Structure, Morphology, and Phase Transitions in CVD Grown VO₂ and V₂O₃ Nanostructures. *Chem. Mater.* **2017**, *29*, 5877–5885.
- (34) Graf, D.; Queralto, A.; Lepcha, A.; Appel, L.; Frank, M.; Mathur, S. Electrospun SrNb₂O₆ Photoanodes from Single-Source Precursors for Photoelectrochemical Water Splitting. *Sol. Energy Mater. Sol. Cells* **2020**, *210*, No. 110485.
- (35) Straub, M. D.; Leduc, J.; Frank, M.; Raaf, A.; Lohrey, T. D.; Minasian, S. G.; Mathur, S.; Arnold, J. Chemical Vapor Deposition of Phase-Pure Uranium Dioxide Thin Films from Uranium(IV) Amidate Precursors. *Angew. Chem., Int. Ed.* **2019**, *58*, 5749–5753.
- (36) Wijk, M.; Norrestam, R.; Nygren, M.; Westin, G. Synthesis, Characterization, and Structural Determination of the Bimetallic Alkoxide ErAl₃(OC₃H₇)₁₂. *Inorg. Chem.* **1996**, *35*, 1077–1079.
- (37) Westin, G.; Kritikos, M.; Wijk, M. Synthesis and Properties of Erbium Isopropoxides: Structural Characterization of Er₃O(OPr)₁₃. *J. Solid State Chem.* **1998**, *141*, 168–176.
- (38) Kritikos, M.; Wijk, M.; Westin, G. [Er₂Al₂(O'Pr)₁₂(HO'Pr)₂], a Novel Heterobimetallic Alkoxide. *Acta Crystallogr., Sect. C: Cryst. Struct. Commun.* **1998**, *54*, 576–578.
- (39) Moustiakimov, M.; Kritikos, M.; Westin, G. Nd[Al(O'PrO)₄]₃, a Novel Tetranuclear Alkoxide Forming Merohedrally Twinned Crystals. *Acta Crystallogr., Sect. C: Cryst. Struct. Commun.* **2001**, *57*, 515–516.
- (40) Berger, E.; Westin, G. Structure of a Hepta-Nuclear Termetallic Oxo-Alkoxide: Eu₃K₃TiO₂(OBU)₁₁(OMe/OH)(HOBU). *J. Sol-Gel Sci. Technol.* **2010**, *53*, 681–688.
- (41) Sharma, M. K.; Sharma, M.; Singh, A.; Mehrotra, R. C. Synthesis and Characterization of Heterobimetallic Isopropoxides of Bismuth (III). *Indian J. Chem., Sect. A: Inorg., Phys. Theor. Anal. Chem.* **2001**, *40*, 1226–1228.
- (42) Mishra, S.; Agarwal, R.; Singh, A. Four Novel Classes of Heterobimetallic Isopropoxides of Chromium(III). *Transition Met. Chem.* **2002**, *27*, 712–715.
- (43) Mathur, S.; Shen, H.; Rapalaviciute, R.; Kareiva, A.; Donia, N. Kinetically Controlled Synthesis of Metastable YAlO₃ through Molecular Level Design. *J. Mater. Chem.* **2004**, *14*, 3259–3265.
- (44) Hemmer, E.; Huch, V.; Adlung, M.; Wickleder, C.; Mathur, S. Homo- and Heterometallic Terbium Alkoxides - Synthesis, Characterization and Conversion to Luminescent Oxide Nanostructures. *Eur. J. Inorg. Chem.* **2011**, *2011*, 2148–2157.
- (45) Veith, M.; Mathur, S.; Huch, V. Designed Synthesis and Molecular Structure of the First Heterotermetallic Alkoxide. *J. Am. Chem. Soc.* **1996**, *118*, 903–904.
- (46) Giaquinta, D. M.; Davis, W. M.; zur Loye, H. C. Structure of Indium Iron Oxide. *Acta Crystallogr., Sect. C: Cryst. Struct. Commun.* **1994**, *50*, 5–7.
- (47) Downie, L. J.; Goff, R. J.; Kockelmann, W.; Forder, S.; Parker, J. E.; Morrison, F. D.; Lightfoot, P. Structural, Magnetic and Electrical Properties of the Hexagonal Ferrites MFeO₃ (M = Y, Yb, In). *J. Solid State Chem.* **2012**, *190*, 52–60.
- (48) Zhang, B.; Seki, M.; Zhou, H.; Chen, J.; Tabata, H. InFeO₃ Photoelectrode with Two-Dimensional Superlattice for Visible- and Ultraviolet-Light-Driven Water Splitting. *APL Mater.* **2020**, *8*, 051107.
- (49) Fujita, K.; Kawamoto, T.; Yamada, I.; Hernandez, O.; Hayashi, N.; Akamatsu, H.; Lafargue-Dit-Hauret, W.; Rocquefelte, X.; Fukuzumi, M.; Manuel, P.; Studer, A. J.; Knee, C. S.; Tanaka, K. LiNbO₃-Type InFeO₃: Room-Temperature Polar Magnet without

Second-Order Jahn-Teller Active Ions. *Chem. Mater.* **2016**, *28*, 6644–6655.

(50) Lima, A. F.; Lalic, M. V. Comparative Study of Magnetic and Electronic Properties of Room-Temperature Polar Magnets ScFeO_3 and InFeO_3 . *Int. J. Quantum Chem.* **2019**, *119*, e25846.

(51) Liu, S.; Wang, R.; Wang, C.; Wang, F.; Xu, Y.; Sun, K.; Hao, X. Asymmetric Covalence Bonding between In 5s and O 2p States in Ferroelectric InFeO_3 . *J. Phys. Chem. Solids* **2018**, *122*, 1–7.

(52) Ikeda, N.; Ohsumi, H.; Ohwada, K.; Ishii, K.; Inami, T.; Kakurai, K.; Murakami, Y.; Yoshii, K.; Mori, S.; Horibe, Y.; Kitô, H. Ferroelectricity from Iron Valence Ordering in the Charge-Frustrated System LuFe_2O_4 . *Nature* **2005**, *436*, 1136–1138.

(53) Oka, K.; Azuma, M.; Hayashi, N.; Muranaka, S.; Narumi, Y.; Kindo, K.; Ayukawa, S.; Kato, M.; Koike, Y.; Shimakawa, Y.; Takano, M. Charge and Magnetic Orderings in the Triangular-Lattice Antiferromagnet InFe_2O_4 . *J. Phys. Soc. Jpn.* **2008**, *77*, 064803.

(54) Akaiwa, K.; Kaneko, K.; Fujita, S.; Chikoidze, E.; Dumont, Y. Room Temperature Ferromagnetism in Conducting α - $(\text{In}_{1-x}\text{Fe}_x)_2\text{O}_3$ Alloy Films. *Appl. Phys. Lett.* **2015**, *106*, 1–5.

(55) Shannon, R. D.; Vincent, H.; Kjekshus, A.; Rakke, T.; Allen, G. C.; Warren, K. D. *Chemical Bonding in Solids*; Springer-Verlag: Berlin, 1974.

(56) Appel, L.; Fiz, R.; Tyrra, W.; Mathur, S. New Iso-Propoxides, Tert-Butoxides and Neo-Pentoxides of Niobium(v): Synthesis, Structure, Characterization and Stabilization by Trifluoroheteroarylalkenolates and Pyridine Ligands. *Dalt. Trans.* **2012**, *41*, 1981–1990.

(57) Leduc, J.; Ravithas, R.; Rathgeber, L.; Mathur, S. New Air-Stable Uranium(IV) Complexes with Enhanced Volatility. *New J. Chem.* **2015**, *39*, 7571–7574.

(58) Brückmann, L.; Tyrra, W.; Stucky, S.; Mathur, S. Novel Air-Stable and Volatile Bis(Pyridylalkenolato)Palladium(II) and -Platinum(II) Derivatives. *Inorg. Chem.* **2012**, *51*, 536–542.

(59) Heidemann, T.; Mathur, S. Air-Stable and Volatile Bis(Pyridylalkenolato)Germanium(II), -Tin(II), and -Lead(II) Complexes. *Eur. J. Inorg. Chem.* **2014**, *2014*, 506–510.

(60) Fornalczyk, G.; Valldor, M.; Mathur, S. Monomeric Iron Heteroarylalkenolates: Structural Design Concepts and Investigations on Their Application in Chemical Vapor Deposition. *Cryst. Growth Des.* **2014**, *14*, 1811–1818.

(61) Büyükyazi, M.; Hegemann, C.; Lehnen, T.; Tyrra, W.; Mathur, S. Molecular Co(II) and Co(III) Heteroarylalkenolates as Efficient Precursors for Chemical Vapor Deposition of Co_3O_4 Nanowires. *Inorg. Chem.* **2014**, *53*, 10928–10936.

(62) Schläfer, J.; Graf, D.; Fornalczyk, G.; Mettenbörger, A.; Mathur, S. Fluorinated Cerium(IV) Enaminolates: Alternative Precursors for Chemical Vapor Deposition of CeO_2 Thin Films. *Inorg. Chem.* **2016**, *55*, 5422–5429.

(63) Appel, L.; Leduc, J.; Webster, C. L.; Ziller, J. W.; Evans, W. J.; Mathur, S. Synthesis of Air-Stable, Volatile Uranium(IV) and (VI) Compounds and Their Gas-Phase Conversion to Uranium Oxide Films. *Angew. Chem., Int. Ed.* **2015**, *54*, 2209–2213.

(64) Giebelhaus, I.; Müller, R.; Tyrra, W.; Pantenburg, I.; Fischer, T.; Mathur, S. First Air Stable Tin(II) β -Heteroarylalkenolate: Synthesis, Characterization and Application in Chemical Vapor Deposition. *Inorg. Chim. Acta* **2011**, *372*, 340–346.

(65) Leduc, J.; Goenuellue, Y.; Ghamgosar, P.; You, S.; Mouzon, J.; Choi, H.; Vomiero, A.; Grosch, M.; Mathur, S. Electronically-Coupled Phase Boundaries in α - $\text{Fe}_2\text{O}_3/\text{Fe}_3\text{O}_4$ Nanocomposite Photoanodes for Enhanced Water Oxidation. *ACS Appl. Nano Mater.* **2019**, *2*, 334–342.

(66) Nodari, I.; Alebouyeh, A.; Brice, J. F.; Gerardin, R.; Evrard, O. Caracterisation de Nouveau Ferrites d'indium: $\text{In}_2\text{Fe}_4\text{O}_9$ et InFeO_3 . *Mater. Res. Bull.* **1988**, *23*, 1039–1044.

(67) Machala, L.; Zboril, R.; Gedanken, A. Amorphous Iron(III) Oxide - A Review. *J. Phys. Chem. B* **2007**, *111*, 4003–4018.

(68) Stadler, D.; Mueller, D. N.; Brede, T.; Duchoň, T.; Fischer, T.; Sarkar, A.; Giesen, M.; Schneider, C. M.; Volkert, C. A.; Mathur, S. Magnetic Field-Assisted Chemical Vapor Deposition of Iron Oxide Thin Films: Influence of Field – Matter Interactions on Phase

Composition and Morphology. *J. Phys. Chem. Lett.* **2019**, *10*, 6253–6259.

(69) Kim, D. H.; Lee, H. J.; Kim, G.; Koo, Y. S.; Jung, J. H.; Shin, H. J.; Kim, J. Y.; Kang, J. S. Interface Electronic Structures of BaTiO_3 @X Nanoparticles ($X = \gamma\text{-Fe}_2\text{O}_3, \text{Fe}_3\text{O}_4, \alpha\text{-Fe}_2\text{O}_3$, and Fe) Investigated by XAS and XMCD. *Phys. Rev. B: Condens. Matter Mater. Phys.* **2009**, *79*, 2–5.

(70) Cho, D. Y.; Kim, J. Y.; Park, B. G.; Rho, K. J.; Park, J. H.; Noh, H. J.; Kim, B. J.; Oh, S. J.; Park, H. M.; Ahn, J. S.; Ishibashi, H.; Cheong, S. W.; Lee, J. H.; Murugavel, P.; Noh, T. W.; Tanaka, A.; Jo, T. Ferroelectricity Driven by γ D⁰-Ness with Rehybridization in YMnO_3 . *Phys. Rev. Lett.* **2007**, *98*, 1–4.

(71) Asokan, K.; Dong, C. L.; Bao, C. W.; Tsai, H. M.; Chiou, J. W.; Chang, C. L.; Pong, W. F.; Duran, P.; Moure, C.; Peña, O. Comparison of Electronic Structures of Orthorhombic and Hexagonal Manganites Studied by X-Ray Absorption Spectroscopy. *Solid State Commun.* **2005**, *134*, 821–826.

(72) Seki, M.; Konya, T.; Inaba, K.; Tabata, H. Epitaxial Thin Films of InFe_2O_4 and InFeO_3 with Two-Dimensional Triangular Lattice Structures Grown by Pulsed Laser Deposition. *Appl. Phys. Express* **2010**, *3*, 105801.

(73) Yamamoto, N.; Takagi, H.; Katsufuji, T.; Masaki, M.; Mori, S.; Moritomo, Y. Dielectric and Magnetic Anomalies and Spin Frustration in Hexagonal RMnO_3 ($R = \text{Y, Yb, and Lu}$). *Phys. Rev. B: Condens. Matter Mater. Phys.* **2001**, *64*, 1–6.

(74) Masuno, A.; Ishimoto, A.; Moriyoshi, C.; Hayashi, N.; Kawaji, H.; Kuroiwa, Y.; Inoue, H. Weak Ferromagnetic Transition with a Dielectric Anomaly in Hexagonal $\text{Lu}_{0.5}\text{Sc}_{0.5}\text{FeO}_3$. *Inorg. Chem.* **2013**, *52*, 11889–11894.

(75) Altomare, A.; Cascarano, G.; Giacovazzo, C.; Guagliardi, A.; Burla, M. C.; Polidori, G.; Camalli, M. Istituto Di Ricerca per Io Sviluppo Di. *J. Appl. Crystallogr.* **1994**, *27*, 435–435.

(76) Sheldrick, G. M. A Short History of SHELX. *Acta Crystallogr., Sect. A: Found. Crystallogr.* **2008**, *A64*, 112–122.

(77) Farrugia, L. J. WinGX Suite for Small-Molecule Single-Crystal Crystallography DISCUS, a Program for Diffuse Scattering and Defect Structure Simulations \pm Update PowderX: Windows-95-Based Program for Powder X-Ray Diffraction Data Processing. *J. Appl. Crystallogr.* **1999**, *32*, 837–838.

(78) Farrugia, L. J. WinGX and ORTEP for Windows: An Update. *J. Appl. Crystallogr.* **2012**, *45*, 849–854.

(79) Klinger, M. More Features, more tools, more CrystBox. *J. Appl. Crystallogr.* **2017**, *50*, 1226–1234.